Nano-Micro Letters

ISSN 2311-6706
e-ISSN 2150-5551
CN 31-2103/TB

ARTICLE

https://doi.org/10.1007/s40820-021-00744-x

Cite as
Nano-Micro Lett.
(2022) 14:20

Received: 15 July 2021
Accepted: 8 October 2021

Three-Phase Heterojunction NiMo-Based Nano-Needle for Water Splitting at Industrial Alkaline Condition

Guangfu Qian[1], Jinli Chen[1], Tianqi Yu[1], Jiacheng Liu[1], Lin Luo[1], Shibin Yin[1] ✉

HIGHLIGHTS

- Three-phase heterojunction can adjust the ΔG of H/O-intermediates to boost catalytic activity.
- At ± 1000 mA cm^{-2}, Ni/MoO_2@CN exhibits low hydrogen/oxygen evolution reaction overpotentials (267/420 mV).
- Ni/MoO_2@CN used as bifunctional electrodes can work at 1000 mA cm^{-2} for 330 h in 6.0 M KOH + 60 °C condition.

ABSTRACT Constructing heterojunction is an effective strategy to develop high-performance non-precious-metal-based catalysts for electrochemical water splitting (WS). Herein, we design and prepare an N-doped-carbon-encapsulated Ni/MoO_2 nano-needle with three-phase heterojunction (Ni/MoO_2@CN) for accelerating the WS under industrial alkaline condition. Density functional theory calculations reveal that the electrons are redistributed at the three-phase heterojunction interface, which optimizes the adsorption energy of H- and O-containing intermediates to obtain the best ΔG_{H^*} for hydrogen evolution reaction (HER) and decrease the ΔG value of rate-determining step for oxygen evolution reaction (OER), thus enhancing the HER/OER catalytic activity. Electrochemical results confirm that Ni/MoO_2@CN exhibits good activity for HER (η_{-10} = 33 mV, η_{-1000} = 267 mV) and OER (η_{10} = 250 mV, η_{1000} = 420 mV). It shows a low potential of 1.86 V at 1000 mA cm^{-2} for WS in 6.0 M KOH solution at 60 °C and can steadily operate for 330 h. This good HER/OER performance can be attributed to the three-phase heterojunction with high intrinsic activity and the self-supporting nano-needle with more active sites, faster mass diffusion, and bubbles release. This work provides a unique idea for designing high efficiency catalytic materials for WS.

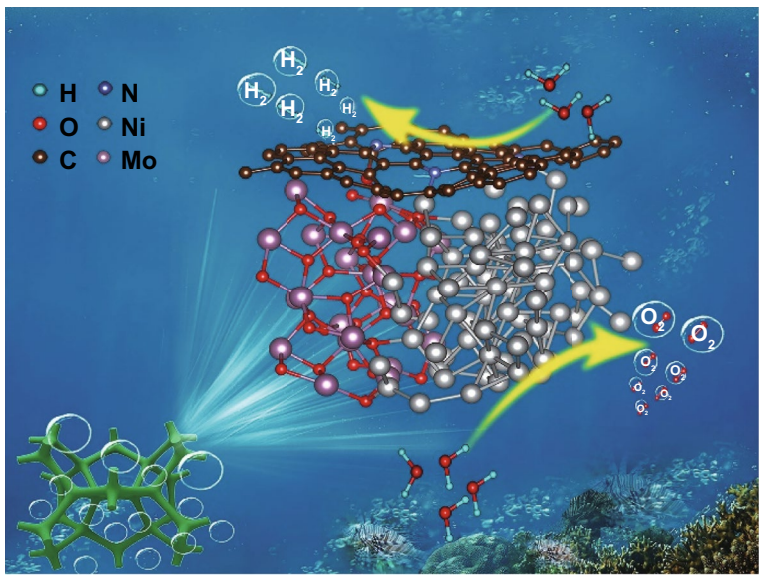

KEYWORDS Three-phase heterojunction; Interfacial electronic redistribution; Catalyst; Large current density; Water splitting

✉ Shibin Yin, yinshibin@gxu.edu.cn
[1] College of Chemistry and Chemical Engineering, State Key Laboratory of Processing for Non-Ferrous Metal and Featured Materials, Guangxi University, 100 Daxue Road, Nanning 530004, People's Republic of China

Published online: 09 December 2021

1 Introduction

Electrochemical water splitting (WS) is considered as a green and convenient method for producing hydrogen (H_2) [1–4]. However, the practical water electrolysis is limited by the sluggish kinetics at cathode (hydrogen evolution reaction, HER) and anode (oxygen evolution reaction, OER) [5–11]. For industrial WS catalyst, these requirements must be met: (1) stable and high active sites at large current density [12]; (2) continuous intensive gas evolution [13, 14]; (3) fast electron transfer [15, 16]; (4) low-cost and accessibility [17, 18]. Although some progress has been made, it is still a challenge to explore high-performance WS catalysts, especially in industrial environment.

The strategies, such as constructing heterojunction [19], fabricating carbon-encapsulating structure [20, 21], and manufacturing defects [22], are demonstrated to improve the WS performance of 3D transition-metals-based (TMB) catalysts. Notably, heterojunction is widely studied for enhancing the WS intrinsic activity through adjusting the electronic structure of catalysts [23, 24]. Mu et al. synthesized Mo-doped Ni_3S_2/Ni_xP_y heterojunction, which optimizes the absorption energy of H- and O-containing intermediates to promote the WS catalytic process [25]. Jiao et al. [26] prepared the heterojunction of Co and nitrogen-rich nitride, which induces its interfacial electronic redistribution to obtain the optimal H* absorption and decrease the dissociation energy barrier.

Furthermore, carbon-encapsulated 3D TMB materials as a kind of heterojunction can not only modulate the electronic structure to boost HER/OER catalytic activity, but also avoid metal corrosion in harsh electrolyte to improve the stability [27]. Deng et al. [28] proved that the surface electronic structure of FeNi alloy with ultrathin graphene layer is adjusted to obtain the good OER performance. Despite the significant progress, most of them are still far from the practical current density (≥ 500 mA cm^{-2}). In our previous work, the graphene-coated NiCo alloy coupled with NiCoMoO and self-supported on 3D nickel foam (NiCo@C–NiCoMoO/NF) was synthesized to improve the intrinsic activity and stability at large current density (≥ 500 mA cm^{-2}), which is different from other carbon-encapsulated 3D TMB materials due to the unique metal oxide anchoring alloy structure. Nevertheless, the understanding of its active sites is still not deep enough. Thus, developing 3D TMB materials with excellent WS performance at large current density and investigating the mechanism of its high intrinsic activity are significant but challenging.

Besides, in order to improve WS stability at large current density, constructing a reasonable structure (nanowires, nanosheets, etc.) on 3D porous substrate (e.g., NF) is significant, which can accelerate the mass transfer and bubbles escape during the electrochemical reaction process, and provide large specific surface area to expose abundant active sites [15, 29]. MoS_2/Ni_3S_2 heterostructure nanowires self-supported on NF were constructed by Cheng et al. [30]. It exhibits a small overpotential of 182 mV at 500 mA cm^{-2} for HER, which is comparable to Pt/C.

Inspired by the above strategies, the N-doped-carbon-coated Ni/MoO_2 nano-needle with three-phase heterojunction (Ni/MoO_2@CN) self-supported on 3D porous NF is rationally engineered and synthesized for the first time, and the HER/OER intrinsic activity is further investigated by density functional theory (DFT) calculations. This novel structure has the following advantages: (1) The electronic structure of N-doped-carbon (CN), Ni, and MoO_2 can be optimized at three-phase heterojunction interface for adjusting the adsorption energy of H- and O-containing intermediates, which can be beneficial to obtain the best H* Gibbs free energy (ΔG_{H^*}) for HER and decrease the Gibbs free energy (ΔG) value of rate-determining step (RDS) for OER, thus enhancing the HER/OER intrinsic activity and electron transfer ability under a large current density [31]. (2) CN can prevent metal corrosion in electrolyte to boost catalytic stability [27, 32]. (3) Nano-needles self-supported on 3D NF with meso/macroporous structure can provide large specific surface area to expose more active sites for reducing the energy barriers of WS [33]. Furthermore, it is beneficial to mass diffusion and bubbles release at large current density, thus improving the WS performance [34].

Benefitting from the synergistic effect among the CN, Ni, and MoO_2 at the three-phase heterojunction interface, as well as the unique self-supporting nano-needle structure, the prepared Ni/MoO_2@CN exhibits low overpotentials at ± 10 and ± 1000 mA cm^{-2} for HER ($\eta_{-10} = 33$ mV, $\eta_{-1000} = 267$ mV) and OER ($\eta_{10} = 250$ mV, $\eta_{1000} = 420$ mV). As for WS, it shows a low potential (1.86 V) at 1000 mA cm^{-2} in 6.0 M KOH solution at 60 °C with an ignorable depletion of activity after 330 h testing, showing excellent stability. Therefore, this work provides a promising catalyst for WS, and it sheds

https://doi.org/10.1007/s40820-021-00744-x

light on developing highly efficient non-precious-metal materials for industrial water electrolysis.

2 Result and Discussion

2.1 DFT Calculations for HER and OER

Firstly, the computational models of Ni/MoO_2@CN, Ni/MoO_2, Ni@CN, MoO_2@CN, and CN are designed (the details are displayed in Fig. S1). Then, the three-phase heterojunction interface synergy effect and HER activity are studied via DFT computations. Particularly, the ΔG_{H^*} and electron distribution for the active atoms are investigated by DFT and density of states (DOS) [35]. Hence, we consider all possible active sites of Ni/MoO_2@CN for HER and calculate their ΔG_{H^*} (Figs. 1a and S2). As shown in Fig. 1a, the ΔG_{H^*} of Ni/MoO_2@CN (0.056 eV) on the Mo-ortho-C between Ni and MoO_2 interface (named as Mo-C1) is close to zero, which is superior to other active sites in Ni/MoO_2@CN model (Figs. 1a and S3). Furthermore, the ΔG_{H^*} value of Mo-C1 in Ni/MoO_2@CN model is better than the ortho-C of MoO_2@CN, Ni@CN, and CN models (Figs. S4–S9), indicating that the three-phase heterojunction interface can effectively adjust the H adsorption energy for ortho-C to obtain the highest HER intrinsic activity.

Afterward, the DOS of CN, MoO_2@CN, and Ni/MoO_2@CN models are used to further confirm the electronic structure of C at the three-phase heterojunction interface. As displayed in Fig. 1b, the strength of this ordinate for CN, MoO_2@CN, and Ni/MoO_2@CN models indicates that the introduction of Ni species can construct the three-phase heterojunction interface to adjust the electronic structure of CN, which optimizes the ΔG_{H^*} of HER. Besides, for revealing the bond capabilities, the crystal orbital Hamilton population (COHP) derived from partial DOS (PDOS) calculation (Fig. 1c, d) are implemented [36]. The energy integral of COHP (ICOHP) of C–H for Ni/MoO_2@CN is − 3.38 (Fig. 1c), which is larger than those in other models (Figs. S5, S7, and S9), suggesting that it has stronger hydrogen adsorption to obtain higher HER catalytic activity [37].

Subsequently, Fig. 2a shows the four-step mechanism processes for OER in alkaline media [38]. The surface of Ni/MoO_2@CN (Fig. 2a), Ni/MoO_2 (Fig. S10), Ni@CN (Fig.

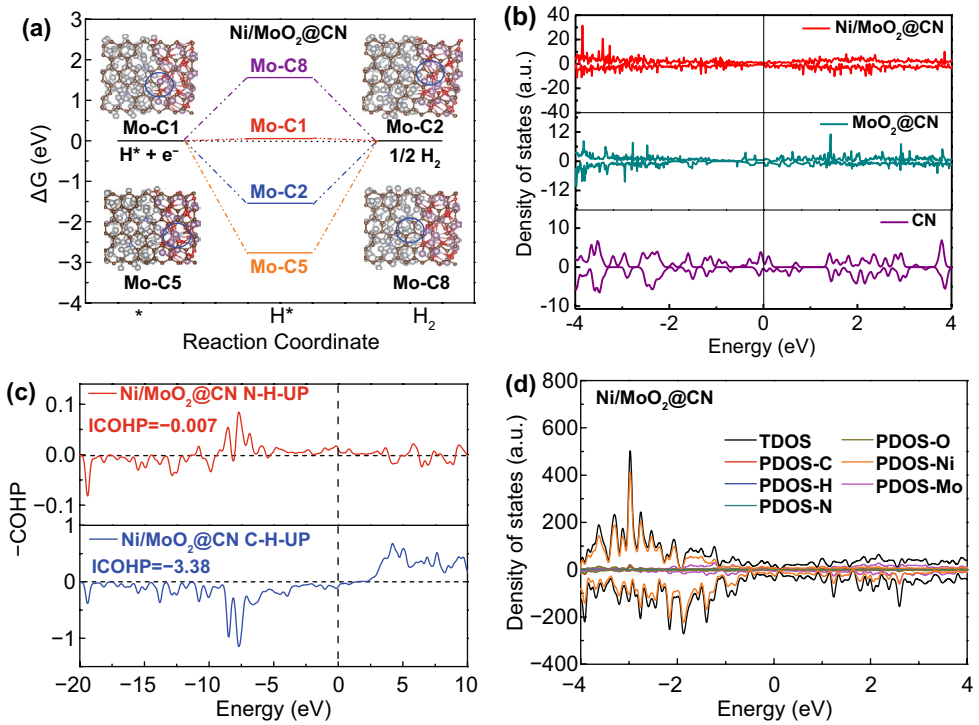

Fig. 1 **a** ΔG_{H^*} calculated at different adsorb sites for Ni/MoO_2@CN model, insert: schematic illustration of H adsorption; **b** PDOS analysis of C for all samples; **c** COHP; and **d** PDOS analysis for the Ni/MoO_2@CN model with the H atom adsorbed on the sites

S11), MoO_2@CN (Fig. S12), and CN (Fig. S13) models displays the adsorption of OER intermediates. During the four OER reaction processes, the ΔG is employed to investigate the intrinsic activity, and the largest ΔG value indicates the rate-determining step (RDS) [39]. As shown in Fig. 2b, step 4 is RDS for Ni/MoO_2, which exhibits ΔG value of 2.39 eV. For Ni/MoO_2@CN, we combine CN with Ni/MoO_2 to form the three-phase heterogeneous junction interface, the RDS is changed from step 4 to step 2, and its ΔG value is reduced to 1.65 eV. The smaller ΔG value of Ni/MoO_2@CN implies the faster reaction kinetics to obtain lower potential during the OER process, and it is better than other catalysts in this work (Figs. S14–S16). Besides, it is found that the Ni *d*-band center of Ni/MoO_2@CN exhibits a negative shift compared with Ni/MoO_2 (Fig. 2c), which is also good for adjusting the adsorption of O-intermediates. Meanwhile, the PDOS results (Fig. 2c) demonstrate that the electrons are transferred from Ni to CN, indicating that the three-phase

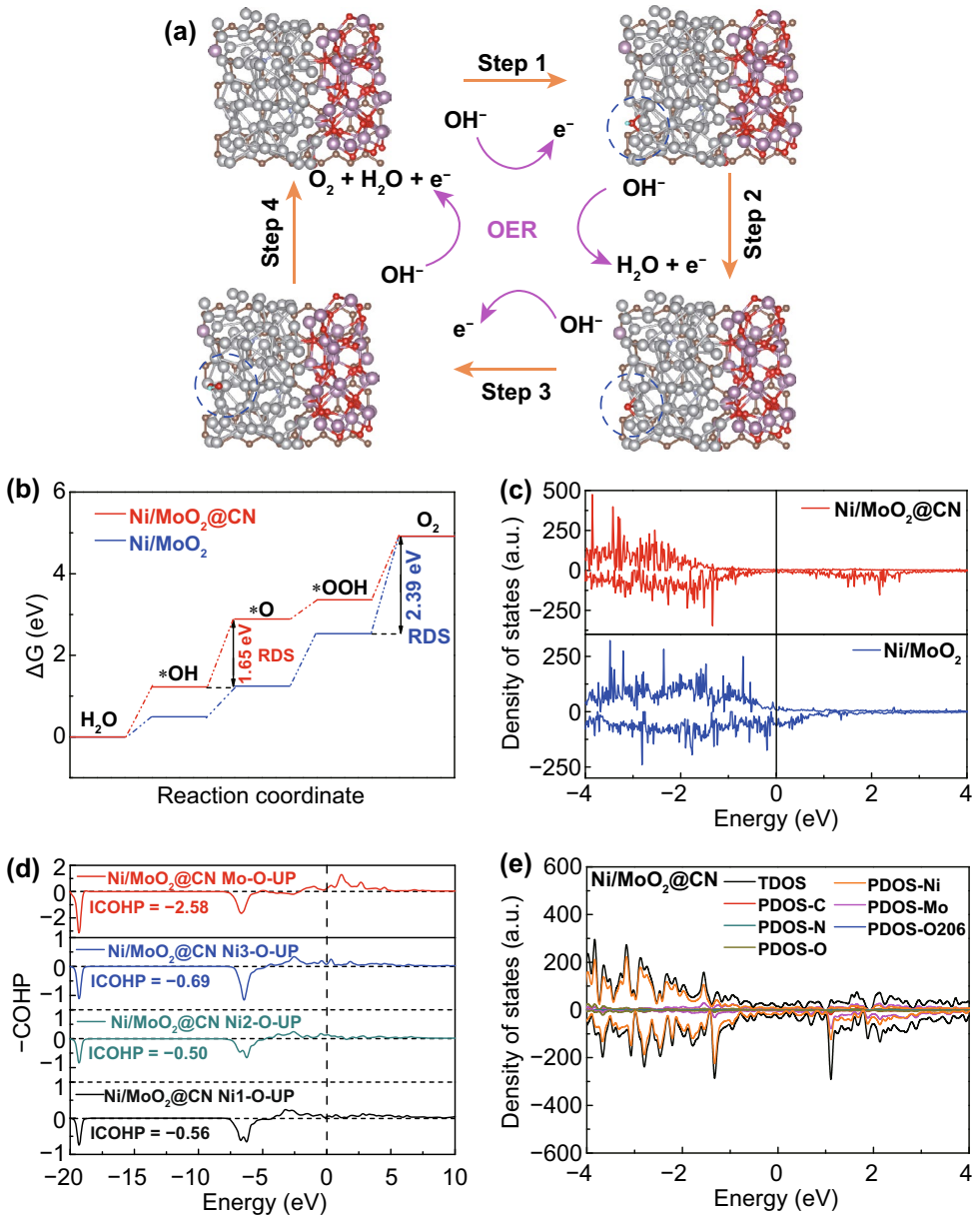

Fig. 2 **a** Schematic illustration of the *OH, *O, and *OOH adsorption for Ni/MoO_2@CN model; **b** OER reaction pathway for Ni/MoO_2@CN model; **c** PDOS analysis of Ni for all samples; **d** COHP; and **e** PDOS analysis for the Ni/MoO_2@CN model with the O atom adsorbed on the sites

https://doi.org/10.1007/s40820-021-00744-x

heterojunction formed by CN and Ni/MoO_2 exists electron interaction, which could enhance the intrinsic activity for OER.

The COHP (Fig. 2d) is used to uncover the bond capabilities, which is originated from PDOS calculation (Fig. 2e) [40]. When CN combines with Ni/MoO_2 to form the three-phase heterojunction, the strength of interaction between Ni and O can be changed. As shown in Figs. 2d and S17a, the ICOHP (−0.69, −0.50, −0.56) values of Ni/MoO_2@CN for Ni suggest that it possesses better interaction between Ni and O, in relative to ICOHP values (−0.54, −0.54, −0.54) of Ni/MoO_2. Furthermore, the Mo atom has good oxygen adsorption capacity (−2.58) at the three-phase heterojunction interface to provide more O-intermediates to boost the OER intrinsic activity. Thus, the COHP results indicate that the three-phase heterojunction interface composed of Ni, MoO_2, and CN can effectively optimize the desorption of O-containing intermediates to enhance the OER intrinsic activity.

2.2 Physicochemical Characterization

Guided by the DFT predictions, the facile two-step methods (Fig. 3, the detailed steps are shown in Supplementary Information) are used to synthesize the CN layer coated Ni/MoO_2 nano-needle with three-phase heterojunction (Ni/MoO_2@CN) self-supported on 3D porous NF. The powder used for X-ray diffraction (XRD) characterization is obtained from NF that has been treated by ultrasonication rather than directly using NF samples. As shown in Supplementary Figure S18, firstly, the $NiMoO_4$ nano-needle is grown on NF via the solvothermal method, which can be determined by XRD (Supplementary Figure S19). Then, the $NiMoO_4$ nano-needle is reduced by the high temperature (450 °C) calcination in a mixed atmosphere (5% H_2 + 95% Ar) to form the Ni nanoparticle and MoO_2 nano-needle, and this is confirmed by XRD and scanning electron microscopy (SEM, Fig. S20–S21). The reason can be attributed to the different enthalpy of Ni and Mo [41]. Besides, Raman proves the existing of CN, which can be ascribed to the reduction of organic carbon to CN [the ratio of area D and G ($Area_D$ and $Area_G$) is 1.20], this is because the catalysis of Ni atoms (Fig. S22c) [22, 42]. Thus, these results suggest that the catalyst is composed of CN, Ni, and MoO_2.

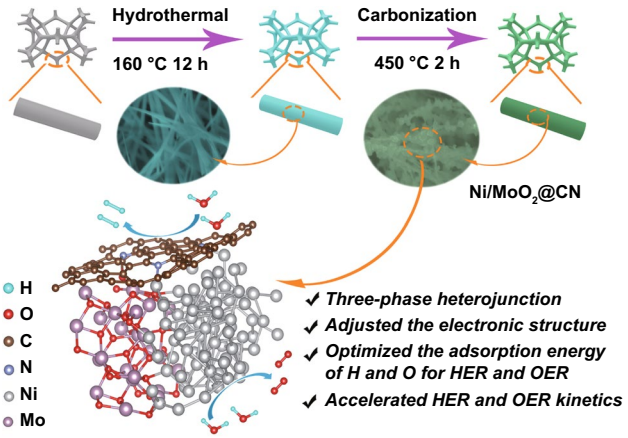

Fig. 3 Synthesis diagram of Ni/MoO_2@CN

Subsequently, the XRD, Raman, and SEM images obtained by annealing the $NiMoO_4$ nano-needle at 350 and 550 °C are shown in Figs. S22–S23, respectively. When it calcined at 350 °C, the characteristic peak intensities of Ni and MoO_2 are too weak. In this case, the morphology of nano-needle is smooth, and the ratio of $Area_D/Area_G$ is 1.10 with less defects of CN. When it calcined at 550 °C, the characteristic peaks of Ni and MoO_2 are replaced by the MoNi alloy, and the morphology of nano-needle is destroyed, under the circumstances, the ratio of $Area_D/Area_G$ is 1.15. Therefore, these results indicate that the temperature plays an important role on the formation of this catalyst.

Then, summarizing the results of XRD, Raman, and SEM (Figs. S22–S23) obtained at different temperatures, the following reason for the formation of catalyst can be proposed: The different enthalpy of Ni and Mo can lead to the segregation of Ni atoms from $NiMoO_4$ to form Ni as well as the reduction of MoO_4^{2-} to MoO_2 at 450 °C, and the segregated Ni can catalyze the organic carbon to form CN. However, when the $NiMoO_4$ nano-needle annealed at 350 °C, due to the low temperature, there is no enough energy to reduce $NiMoO_4$ forming Ni and MoO_2, and the surface organic carbon cannot form CN. And when it calcined at 550 °C, due to the high temperature, the Ni and Mo atoms segregate from the $NiMoO_4$ to form the NiMo alloy, but organic carbon cannot form the CN on its surface, mainly attributed to the rapid reduction at such high temperature. Therefore, the $NiMoO_4$ calcined at 350 and 550 °C exhibits lower HER/OER intrinsic activity (Figs. S29 and S41).

Subsequently, the transmission electron microscopy (TEM) and high-resolution TEM (HRTEM) are employed to reveal the three-phase heterojunction and lattice fringe of Ni/MoO_2@CN. As shown in Fig. 4a–c, the 0.208 nm (111) of Ni nanoparticle couples with the 0.242 nm (200) of MoO_2 nano-needle (consistent with XRD results). Obviously, the carbon layers are coated on the surface of Ni (≈3 layers, Fig. 4b) and MoO_2 (≈2 layers, Fig. 4d), which can efficiently optimize the electron distribution to enhance the HER/OER intrinsic activity, and this is also confirmed by DFT [43, 44]. Furthermore, carbon layers can avoid metal corrosion in electrolyte to improve the electrochemical stability [27]. More importantly, a clear heterojunction exists between the Ni nanoparticle and MoO_2 nano-needle (Fig. 4c, d), which can realize the redistribution of electrons at the interface for further optimizing the adsorption energy of H- and O-containing intermediates to boost the HER/OER intrinsic activity [25]. Additionally, heterojunction can enhance the electron transfer ability to improve the WS performance at large current density [45]. The high-angle annular dark-field scanning TEM (HAADF-STEM) and elemental mapping images sugggest the uniform distribution of C, N, O, Ni, and Mo on the Ni/MoO_2@CN (Fig. 4e–j).

X-ray photoelectron spectroscopy (XPS) is used to evaluate the elemental compositions and valance states. XPS survey spectrum of Ni/MoO_2@CN is shown in Fig. S24a, which confirms the existence of Ni, C, Mo, N, and O elements. In Fig. S24b, c, HRXPS of O 1*s* and C 1*s* is located at Mo–O (530.8 eV), absorbed-O (532.1 eV), C=O (288.8 eV), C–N (286.3 eV), and C–C (284.8 eV). For N 1*s* spectrum, the peaks at 396.1 and 398.6 eV belong to Mo 3*p* and pyridinic-N (Fig. S24d), as known, the doping of N atoms into carbon layer can enhance the HER/OER intrinsic activity [46, 47]. The Ni 2*p* and Mo 3*d* of Ni/MoO_2@CN show a positive shift (≈0.3 eV, Fig. 4k and Table S1) and negative shift (≈0.3 eV, Fig. 4l and Table S2) relative to Ni/MoO_2, respectively, displaying that the CN affects the electronic structure of Ni and MoO_2, and this is in agreement with the DFT predictions.

Furthermore, Ni 2*p* spectrum of Ni/MoO_2@CN presents a positive shift (≈0.5 eV, Fig. 4m and Table S1) relative to Ni@CN, showing that the introduction of MoO_2 can adjust the electronic structure of Ni@CN. In Fig. 4n and Table S2, Mo 3*d* spectrum of Ni/MoO_2@CN exhibits a negative shift (≈0.5 eV) as against to MoO_2@CN, which suggests that the electronic structure of Mo 3*d* for MoO_2@CN is also affected, because it is coupled with Ni@CN to form the three-phase heterojunction interface. In contrast, as displayed in Fig. S25a, b, Ni 2*p*, and Mo 3*d* peaks of Ni@CN + MoO_2@CN hybrids (mixing the Ni@CN and MoO_2@CN together) are the same as Ni@CN and MoO_2@CN, respectively, indicating that the mechanical mixing cannot affect the binding energy. However, compared with the Ni@CN + MoO_2@CN hybrids, the Ni 2*p* and Mo 3*d* peaks of Ni/MoO_2@CN present positive and negative shift, respectively. These results demonstrate that coupling Ni@CN with MoO_2@CN to form the three-phase heterojunction interface can lead to the strong electronic interaction, thus adjusting the absorption/desorption of H/O-intermediates to enhance the intrinsic activity [48], which is consistent with DFT calculation results.

It can be seen from the above results that there is indeed a three-phase heterojunction between Ni, MoO_2, and CN. This unique three-phase heterojunction can make the interfacial electronic redistribution of Ni, MoO_2, and CN, thus providing lots of defects to form abundant active sites for reducing the WS reaction energy barrier. Furthermore, the nano-needle self-supporting on 3D NF can expose more active sites to further increase WS catalytic activity, and it is also beneficial for mass diffusion at large current density to improve the WS performance.

2.3 HER Catalytic Performance

Based on the guidance of DFT results and the unique three-phase heterojunction of Ni/MoO_2@CN, HER mechanism can be illustrated in Fig. 5a, and the HER activity is evaluated by the linear sweep voltammetry (LSV) curves with/without *iR*-correction (Fig. S26). As displayed in Fig. 5b, c, the Ni/MoO_2@CN possesses good HER activity with low overpotentials (η_{-10} = 33 mV, η_{-1000} = 267 mV), which is better than that of MoO_2@CN (η_{-10} = 134 mV, η_{-1000} = 430 mV). This result suggests that the introduction of Ni into MoO_2@CN to form the three-phase heterojunction of Ni/MoO_2@CN can greatly enhance the HER activity, and it is consistent with the DFT results. It is also better than that of precursor (η_{-10} = 210 mV, η_{-1000} = 570 mV), NF (η_{-10} = 256 mV, η_{-1000} = 590 mV), and close to Pt/C (η_{-10} = 25 mV, η_{-1000} = 296 mV), and superior to most of the recently reported catalysts (Fig. S27 and Table S3). Furthermore, Ni/MoO_2@CN shows smaller overpotentials

 https://doi.org/10.1007/s40820-021-00744-x

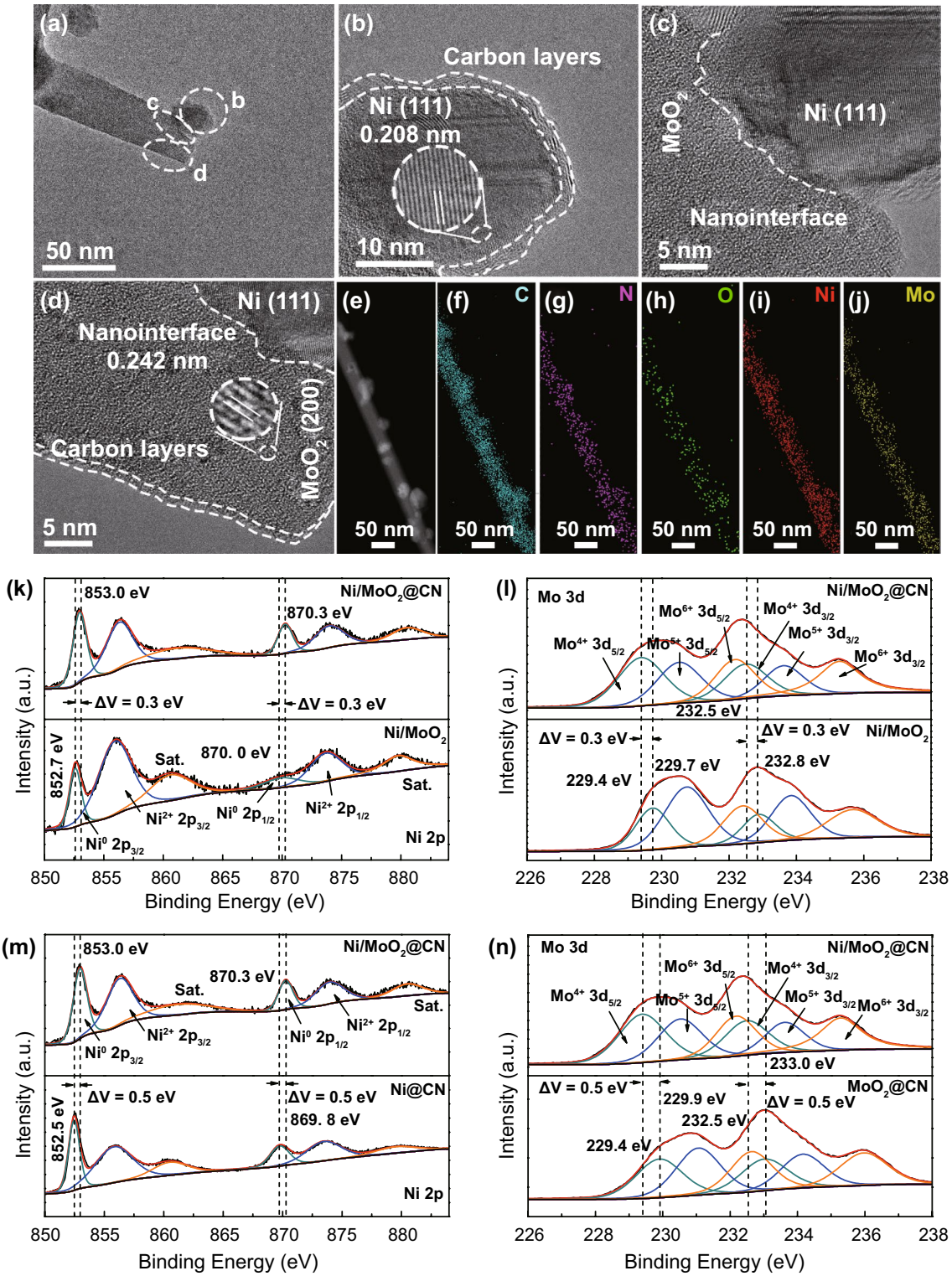

Fig. 4 **a**–**j** TEM, HRTEM, HAADF-STEM, and elemental mapping images of Ni/MoO_2@CN; **k**–**n** HRXPS of Ni 2*p* and Mo 3*d* spectra for Ni/MoO_2@CN, Ni/MoO_2, Ni@CN, and MoO_2@CN

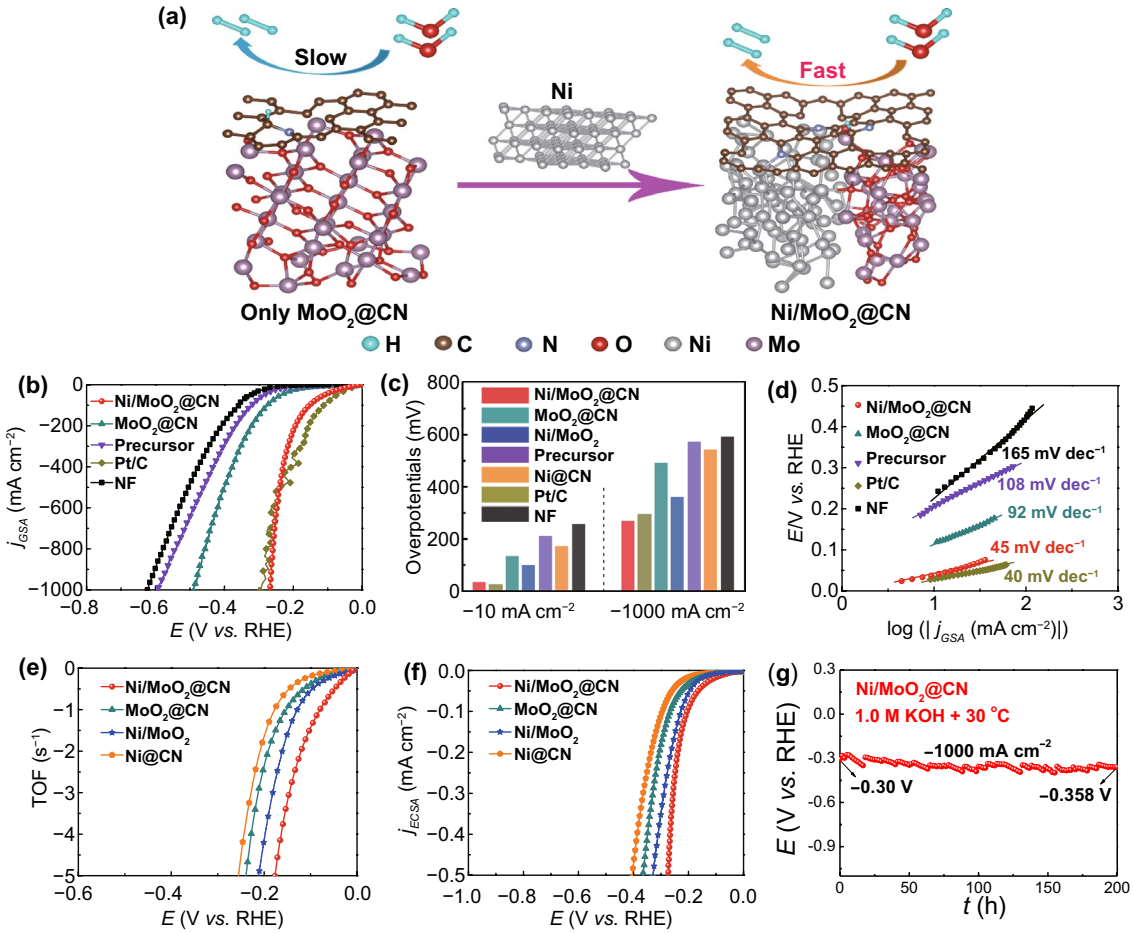

Fig. 5 **a** Schematic diagram of HER mechanism: Ni/MoO_2@CN exhibits better HER kinetics compared to MoO_2@CN; **b** LSV curves; **c** comparison of overpotentials; **d** Tafel plots; **e** TOF curves; **f** ECSA-normalized LSV curves of as-prepared samples; **g** CP curve of Ni/MoO_2@CN

compared with Ni@CN (η_{-10} = 173 mV, η_{-1000} = 474 mV) in Figs. 5c and S28a. This proves that the three-phase heterojunction of Ni/MoO_2@CN synthesized by combining MoO_2 with Ni@CN leads to further optimize the electronic structure of CN for obtaining an outstanding HER intrinsic activity, and it agrees with DFT results. Meanwhile, Ni/MoO_2 needs higher overpotentials (η_{-10} = 100 mV, η_{-1000} = 358 mV) compared with Ni/MoO_2@CN in Figs. 5c and S28a, implying that the CN decorated Ni/MoO_2 can reduce the HER reaction barrier by optimizing the ΔG_{H^*}.

Through above results comparing of Ni/MoO_2@CN, Ni/MoO_2, Ni@CN, and Ni/MoO_2, we can conclude that the interfacial charge redistribution at three-phase heterojunction is good for HER, and the Ni, MoO_2, and CN are all indispensable. Moreover, the sample with a Ni/Mo molar ratio of 1:7 (Fig. S29) and the $NiMoO_4$ annealed at 450 °C (Supplementary Figure S30) exhibits higher HER intrinsic activity, which indicates that the Ni/Mo molar ratio as well as the calcination temperature has an important impact on the HER intrinsic activity.

Figures 5d and S28b show Tafel plots originated from the LSV curves. The Ni/MoO_2@CN exhibits a lower Tafel slope of 45 mV dec^{-1} than those of MoO_2@CN (92 mV dec^{-1}), Ni@CN (85 mV dec^{-1}), Ni/MoO_2 (81 mV dec^{-1}), precursor (108 mV dec^{-1}), NF (165 mV dec^{-1}), and like Pt/C (40 mV dec^{-1}), indicating that Ni/MoO_2@CN obtains faster HER catalytic kinetics. Then, the charge transfer kinetics is analyzed by electrochemical impedance spectroscopy (Fig. S31), and Ni/MoO_2@CN has the smallest charge transfer resistance (R_{ct}) among all samples, implying the fastest

https://doi.org/10.1007/s40820-021-00744-x

charge transfer rate of HER. The superiority of HER reaction kinetics and charge transfer can be ascribed to interface electronic transmission at the three-phase heterojunction among CN, Ni, and MoO_2.

Besides, the turnover frequency (TOF) and electrochemical surface area (ECSA) are used to explore the HER intrinsic activity and the number of active sites, respectively [49]. Cyclic voltammetry (CV) method is used to study the TOF of HER (Fig. S32) [50]. In Fig. 5e and Table S4, Ni/MoO_2@CN possesses the largest TOF value (1.45 s^{-1}) at the overpotential of 100 mV, as compared with MoO_2@CN (0.38 s^{-1}), Ni@CN (0.19 s^{-1}), and Ni/MoO_2 (0.53 s^{-1}), suggesting that Ni/MoO_2@CN has the highest catalytic activity. Besides, it also has the highest TOF values at other overpotentials (Table S5), and it is better than most of the previously reported results in literature (Fig. S33 and Table S6).

ECSA can be evaluated by electrochemical double-layer capacitances (C_{dl}), due to the positive correlation between ECSA and C_{dl} (Fig. S34a–d) [42]. Obviously, Ni/MoO_2@CN exhibits the largest C_{dl} (97.94 mF) in Fig. S34e, which implies that it has the highest density of active sites to accelerate the HER process, and it is also reflected in the ECSA-normalized LSV curves (Fig. 5f). The highest intrinsic activity can be due to the interfacial charge redistribution at the three-phase heterojunction interface, which obtains suitable adsorption energy of H and O-containing intermediates. Besides, the self-supporting nano-needle can provide a large specific surface area to expose more active sites.

Stability is another vital index to evaluate catalyst performance [51], especially at large current density. Ni/MoO_2@CN displays outstanding durability at − 1000 mA cm^{-2} for 200 h with stable release of H_2 bubbles, which is tested by the chronopotentiometry (CP) method (Fig. 5g). Furthermore, the activity before and after the CP test has negligible changes (Fig. S35), implying its good stability. Subsequently, the SEM images (Fig. S36) and HRXPS spectra (Fig. S37) of Ni/MoO_2@CN after the CP test are also obtained, and they almost maintain the original state. The better stability can be attributed to the following reasons: (1) The interfacial charge redistribution at three-phase heterojunction for Ni/MoO_2@CN can accelerate the electron transfer at large current density; (2) Carbon layers could avoid the dissolution of metal in harsh solution; (3) Self-supporting nano-needle enhances the wettability of catalyst to effectively boost the mass diffusion and bubbles release.

2.4 OER Catalytic Performance

The Ni/$NiMoO_2$@CN not only has outstanding HER performance, but also exhibits good OER performance under the same condition; the schematic diagram of the OER mechanism is displayed in Fig. 6a. The OER LSV curves of Ni/MoO_2@CN with/without *iR*-correction are presented in Fig. S38. As shown in Fig. 6b, c, Ni/MoO_2@CN shows higher activity (η_{10} = 250 mV, η_{1000} = 420 mV) than Ni/MoO_2 (η_{10} = 300 mV, η_{1000} = 550 mV), which indicates that the decoration of CN to Ni/$NiMoO_2$ can effectively enhance the OER intrinsic activity. Meanwhile, the overpotentials of Ni/MoO_2@CN are also smaller than that of MoO_2@CN (η_{10} = 310 mV, η_{1000} = 590 mV) and Ni@CN (η_{10} = 323 mV, η_{1000} = 660 mV) in Figs. 6c and S39a. These results indicate that the electronic structures of Ni, Mo, and CN are adjusted by interfacial electronic redistribution at the three-phase heterojunction to further optimize the adsorption of O-intermediates; this is also consistent with the DFT results. Besides, as shown in Fig. 6b, c, the Ni/MoO_2@CN exhibits smaller overpotentials than NF (η_{10} = 345 mV, η_{1000} = 700 mV), precursor (η_{10} = 327 mV, η_{1000} = 650 mV), IrO_2/C (η_{10} = 280 mV, η_{1000} = 540 mV), and even superior to most of the recently reported catalysts (Fig. S40 and Table S7). Moreover, the sample with a Ni/Mo molar ratio of 1:7 (Fig. S41) and the $NiMoO_4$ annealed at 450 °C (Fig. S42) displays the lowest OER overpotential, suggesting that the Ni/Mo molar ratio and calcination temperature play an important role on the OER intrinsic activity.

In addition, the Tafel slope and EIS are used to assess the kinetics of OER (Figs. 6d, S39b and S43). Obviously, Ni/MoO_2@CN displays the smallest Tafel slope and smallest R_{ct} value among all catalysts, which implies its high electron transfer rate and fast kinetics for OER at the three-phase heterojunction interface. Subsequently, the good OER intrinsic activity of Ni/MoO_2@CN is also verified by TOF. The active surface redox sites method is used to study the TOF for OER by calculating the redox surface sites of Ni^{2+}/Ni^{3+} without the capacitive current (Fig. S44) [50]. In Fig. 6e and Table S8, the TOF value of Ni/MoO_2@CN (1.23 s^{-1}) is higher than Ni/MoO_2 (0.28 s^{-1}) and Ni@CN (0.14 s^{-1}) at the overpotential of 300 mV, suggesting its higher intrinsic activity. Besides, it also has higher TOF values at other overpotentials (Table S9), which is better than most of the reported works (Fig. S45 and Table S10).

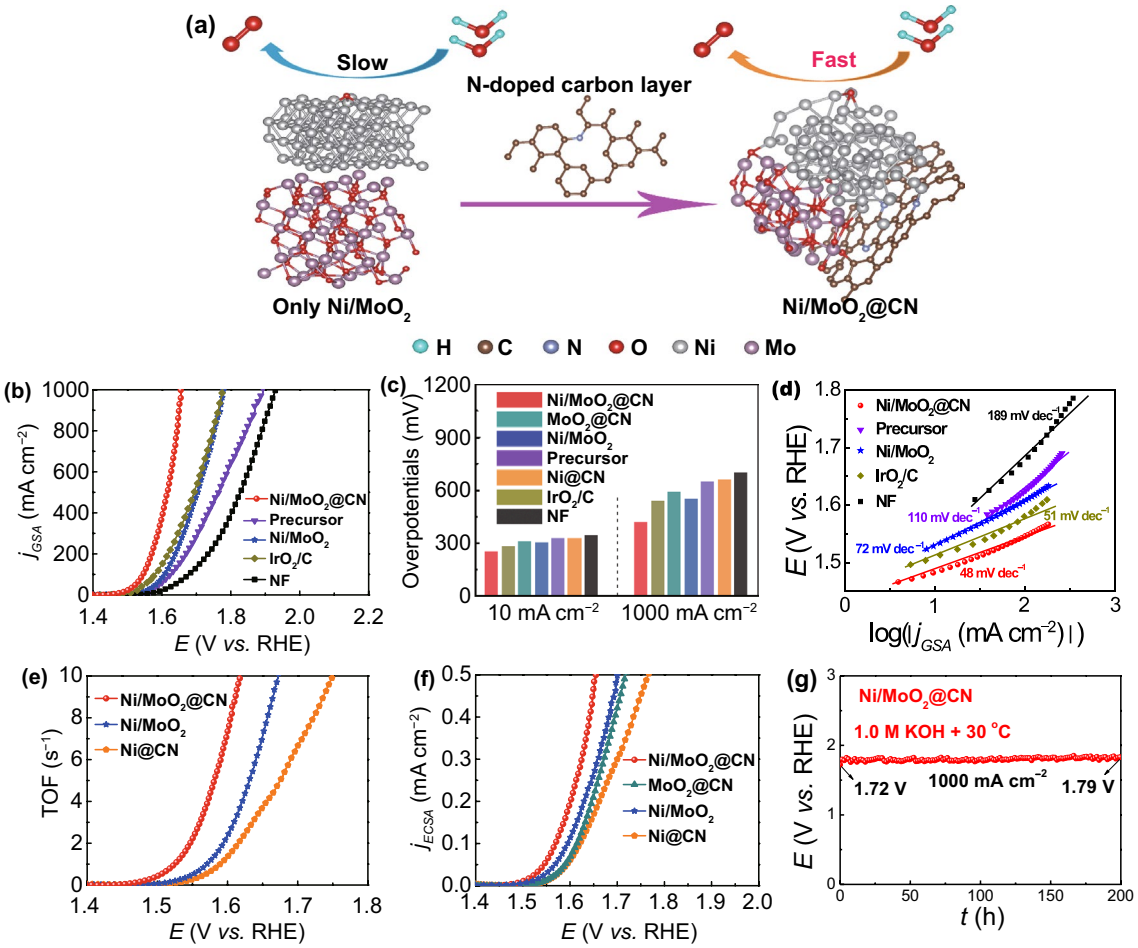

Fig. 6 **a** Schematic diagram of OER mechanism: Ni/MoO_2@CN exhibits better OER kinetics compared to Ni/MoO_2; **b** LSV curves; **c** comparison of overpotentials; **d** Tafel plots; **e** TOF curves; **f** ECSA-normalized LSV curves of as-prepared samples; **g** CP curve of Ni/MoO_2@CN

The current density is normalized by ECSA to further reflect the highest intrinsic activity of Ni/MoO_2@CN (Fig. 6f). The remarkable OER catalytic activity can be ascribed to the following reasons: (1) Interfacial electronic redistribution at three-phase heterojunction interface can be beneficial to optimize the adsorption energy of O-containing intermediates; (2) Interfacial electronic redistribution also can accelerate the charge transfer at large current density to enhance OER activity; (3) Self-supporting nano-needle has a large specific surface area to provide more active sites for boosting the OER performance.

Subsequently, its stability is studied by CP method. Impressively, the Ni/MoO_2@CN maintains good stability for 200 h at 1000 mA cm^{-2} (Fig. 6g); the change of potential is about 70 mV. To investigate its outstanding durability, LSV curves and Nyquist plots before and after stability test are displayed in Fig. S46; the potential at 1000 mA cm^{-2} and R_{ct} value at 1.5 V have minor changes. The reason for the good OER stability should be the same as HER. Then, the change of morphology and elements states after the CP test are studied by SEM and HRXPS. In Fig. S47, SEM images of Ni/MoO_2@CN can keep the primary appearance, indicating its good stability. The HRXPS spectrum of Ni^0 disappeared (Fig. S48), implying that the Ni^0 is oxidized to NiOOH [52], and the Mo^{4+} and Mo^{5+} are also oxidized to Mo^{6+}, which is a common phenomenon during OER process [42]. As reported in literatures [52–54], the generated NiOOH can combine with the Ni to form the heterojunction interface between the NiOOH and Ni during OER process, thus further enhancing the OER intrinsic activity. Meanwhile, according to literatures, the generated Mo^{6+} can be beneficial to the

https://doi.org/10.1007/s40820-021-00744-x

conversion of Ni^{2+} to Ni^{3+} and produce the NiOOH for enhancing the OER intrinsic activity [55, 56].

2.5 WS Catalytic Performance

In considering of the outstanding HER and OER performance of Ni/MoO_2@CN, the WS performance of Ni/MoO_2@CN is also evaluated by two-electrode system to simulate the actual application, and the schematic diagram is shown in Fig. 7a. For comparison, the WS intrinsic activity of Pt/C//IrO_2/C and NF//NF are also measured by the same method with Ni/MoO_2@CN. Under 1.0 M KOH + 30 °C condition, the LSV curve of Ni/MoO_2@CN (1.83 V) as cathode and anode electrodes display a higher activity than Pt/C//IrO_2/C (1.89 V) and NF//NF (2.26 V) at 200 mA cm^{-2} (Fig. 7b). Interestingly, the Ni/MoO_2@CN as bifunctional electrodes can drive the large current density of 500 and 1000 mA cm^{-2} while only requiring 1.92 and 2.02 V, and it is better than most of the reported literatures at 500 mA cm^{-2} (Fig. 7c) [57–65]. Furthermore, it can maintain for 300 h at 1000 mA cm^{-2} (Fig. 7d), exhibiting its excellent stability.

In addition, in order to further evaluate the industrial application potential of Ni/MoO_2@CN, it is applied to WS under the simulated industrial condition (6.0 M KOH + 60 °C). As shown in Fig. 7b, it only requires 1.86 V for Ni/MoO_2@CN to reach 1000 mA cm^{-2} when used as cathode and anode electrodes. It can work stably for 330 h at 1000 mA cm^{-2} with negligible potential change (Fig. 7e), implying that it is a potential material for large-scale hydrogen production. The good WS performance of Ni/MoO_2@CN under the large current density of industrial condition can be attributed to the three-phase heterojunction with high HER/OER intrinsic activity and the self-supporting nanoneedle structure with more active sites, faster bubbles desorption, and the diffusion of electrolyte.

Subsequently, the Faradic efficiency and contact angles (CA) of Ni/MoO_2@CN are surveyed (Figs. 7f, g and S49). The volume–time curve for H_2 and O_2 is obtained by water drainage method at 0, 10, 15, 20, 25, 30, 35, 40, 45, and 50 min measured at 30.0 mA. The volume–time curve for H_2 and O_2 is about 2:1, and they are close to the theoretical values, indicating the nearly 100% Faradic efficiency. Besides, the wettability of catalysts is very important for WS. The CA of Ni/MoO_2@CN and NF with 1.0 M KOH solution are shown in Fig. 7g. Obviously, the CA of Ni/MoO_2@CN (9°) is smaller than NF (45°), suggesting the good gas release and mass transfer. Then, as shown in Fig. S50, the size of H_2 bubbles on NF electrode is much larger than it on Ni/MoO_2@CN electrode, indicating that the H_2 bubbles are easier to desorb from the surface of Ni/MoO_2@CN. Thus, the above results suggest that Ni/MoO_2@CN has good hydrophilicity to enhance the contact with electrolyte and facilitate bubbles desorption for improving the performance of WS.

3 Conclusions

In short, the CN layers encapsulated Ni/MoO_2 nano-needle with three-phase heterojunction is successfully engineered and synthesized. Interestingly, as predicted by DFT results, the electrons are redistributed among the CN, Ni, and MoO_2 for optimizing the adsorption energy of H- and O-containing intermediates in order to obtain the best ΔG_{H^*} for HER and decrease the ΔG value of RDS for OER, thus enhancing the HER/OER intrinsic activity. The physical and electrochemical results are in good agreement with the theoretical predictions. Compared with the XPS results of Ni/MoO_2, Ni@CN, and MoO_2@CN, the peaks of Ni 2*p* and Mo 3*d* for Ni/MoO_2@CN show negative/positive shift, which further demonstrate that there is a strong interaction between CN, Ni, and MoO_2. Therefore, the Ni/MoO_2@CN exhibits good activity for HER (η_{-10} = 33 mV) and OER (η_{10} = 250 mV) compared with Ni/MoO_2 (HER: η_{-10} = 100 mV, OER: η_{10} = 300 mV), MoO_2@CN (HER: η_{-10} = 134 mV, OER: η_{10} = 310 mV), and Ni@CN (HER: η_{-10} = 173 mV, OER: η_{10} = 323 mV). Meanwhile, the three-phase heterojunction can facilitate electronic transfer at large current density and the carbon layers can avoid the metal dissolution in harsh solution. Self-supporting nanoneedle can enhance the wettability of catalyst to effectively boost the mass diffusion and bubbles release. Therefore, it can steadily operate for 330 h at 1000 mA cm^{-2} for WS (6.0 M KOH + 60 °C), suggesting an excellent stability. This work offers a unique idea of designing catalytic materials for industrial electrochemical water splitting.

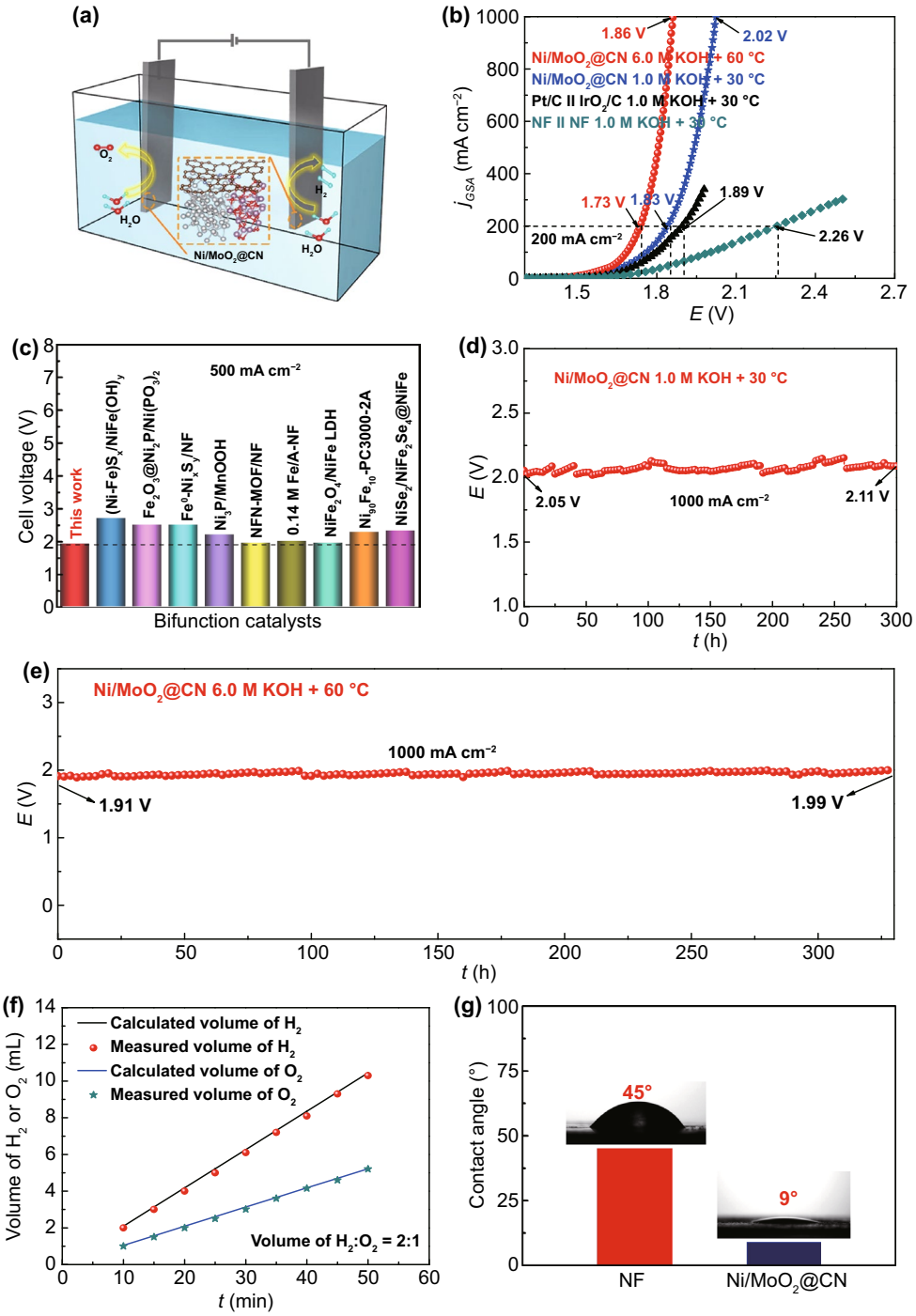

Fig. 7 **a** Schematic diagram of WS for Ni/MoO_2@CN; **b** LSV curves of the samples in 1.0 M KOH + 30 °C, and LSV curve of Ni/MoO_2@CN in 6.0 M KOH + 60 °C; **c** comparison of potentials at 500 mA cm^{-2} of Ni/MoO_2@CN and reported catalysts; CP curves of Ni/MoO_2@CN **d** at 1.0 M KOH + 30 °C and **e** 6.0 M KOH + 60 °C; **f** Volume of H_2 and O_2 measured at 30.0 mA as a function of time for Ni/MoO_2@CN; **g** CA of NF and Ni/MoO_2@CN under 1.0 M KOH. Insert: optical photographs

https://doi.org/10.1007/s40820-021-00744-x

Acknowledgements This work is supported by the National Natural Science Foundation of China (21872040, 22162004), the Hundred Talents Program of Guangxi Universities, the Excellent Scholars and Innovation Team of Guangxi Universities, the Innovation Project of Guangxi Graduate Education (YCBZ2021011), and the High-performance Computing Platform of Guangxi University.

Funding Open access funding provided by Shanghai Jiao Tong University.

Supplementary Information The online version contains supplementary material available at https://doi.org/10.1007/s40820-021-00744-x.

References

1. J. Zhu, L.S. Hu, P.X. Zhao, L.Y.S. Lee, K.Y. Wong, Recent advances in electrocatalytic hydrogen evolution using nanoparticles. Chem. Rev. **120**(2), 851–918 (2020). https://doi.org/10.1021/acs.chemrev.9b00248
2. T. Schuler, T. Kimura, T.J. Schmidt, F.N. Büchi, Towards a generic understanding of oxygen evolution reaction kinetics in polymer electrolyte water electrolysis. Energy Environ. Sci. **13**(7), 2153–2166 (2020). https://doi.org/10.1039/d0ee00673d
3. J.H. Cao, K.X. Wang, J.Y. Chen, C.J. Lei, B. Yang et al., Nitrogen-doped carbon-encased bimetallic selenide for high-performance water electrolysis. Nano-Micro Lett. **11**, 67 (2019). https://doi.org/10.1007/s40820-019-0299-4
4. A. Ali, P.K. Shen, Recent progress in graphene-based nanostructured electrocatalysts for overall water splitting. Electrochem. Energy Rev. **3**, 370–394 (2020). https://doi.org/10.1007/s41918-020-00066-3
5. F. Dionigi, Z.H. Zeng, I. Sinev, T. Merzdorf, S. Deshpande et al., In-situ structure and catalytic mechanism of NiFe and CoFe layered double hydroxides during oxygen evolution. Nat. Commun. **11**, 2522 (2020). https://doi.org/10.1038/s41467-020-16237-1
6. J. Kim, H. Jung, S.M. Jung, J. Hwang, D.Y. Kim et al., Tailoring binding abilities by incorporating oxophilic transition metals on 3D nanostructured Ni arrays for accelerated alkaline hydrogen evolution reaction. J. Am. Chem. Soc. **143**(3), 1399–1408 (2021). https://doi.org/10.1021/jacs.0c10661
7. K. Chen, Z.M. Wang, L. Wang, X.Z. Wu, B.J. Hu et al., Boron nanosheet-supported Rh catalysts for hydrogen evolution: a new territory for the strong metal-support interaction effect. Nano-Micro Lett. **13**, 138 (2021). https://doi.org/10.1007/s40820-021-00662-y
8. A. Hossain, K. Sakthipandi, A.K.M.A. Ullah, S. Roy, Recent progress and approaches on carbon-free energy from water splitting. Nano-Micro Lett. **11**, 103 (2019). https://doi.org/10.1007/s40820-019-0335-4
9. H. Gao, H.H. Yue, F. Qi, B. Yu, W.L. Zhang et al., Few-layered ReS_2 nanosheets grown on graphene as electrocatalyst for hydrogen evolution reaction. Rare Met. **37**, 1014–1020 (2018). https://doi.org/10.1007/s12598-018-1121-z
10. A. Saad, D.Q. Liu, Y.C. Wu, Z.Q. Song, Y. Li et al., Ag nanoparticles modified crumpled borophene supported Co_3O_4 catalyst showing superior oxygen evolution reaction (OER) performance. Appl. Catal. B **298**, 120529 (2021). https://doi.org/10.1016/j.apcatb.2021.120529
11. L. Yan, B. Zhang, J.L. Zhu, Y.Y. Li, P. Tsiakaras et al., Electronic modulation of cobalt phosphide nanosheet arrays via copper doping for highly efficient neutral-pH overall water splitting. Appl. Catal. B **265**, 118555 (2020). https://doi.org/10.1016/j.apcatb.2019.118555
12. T.Y. Kou, S.W. Wang, Y. Li, Perspective on high-rate alkaline water splitting. ACS Mater. Lett. **3**(2), 224–234 (2021). https://doi.org/10.1021/acsmaterialslett.0c00536
13. Y.L. Xu, C. Wang, Y.H. Huang, J. Fu, Recent advances in electrocatalysts for neutral and large-current-density water electrolysis. Nano Energy **80**, 105545 (2021). https://doi.org/10.1016/j.nanoen.2020.105545
14. S.C. Zhang, W.B. Wang, F.L. Hu, Y. Mi, S.Z. Wang et al., 2D CoOOH sheet-encapsulated Ni_2P into tubular arrays realizing 1000 mA cm^{-2}-level-current-density hydrogen evolution over 100 h in neutral water. Nano-Micro Lett. **12**, 140 (2020). https://doi.org/10.1007/s40820-020-00476-4
15. W.J. Jiang, T. Tang, Y. Zhang, J.S. Hu, Synergistic modulation of non-precious-metal electrocatalysts for advanced water splitting. Acc. Chem. Res. **53**(6), 1111–1123 (2020). https://doi.org/10.1021/acs.accounts.0c00127
16. J.M. Cen, E.J. Jiang, Y.Q. Zhu, Z.Y. Chen, P. Tsiakaras et al., Enhanced electrocatalytic overall water splitting over novel one-pot synthesized Ru-MoO_{3-x} and Fe_3O_4-NiFe layered double hydroxide on Ni foam. Renew. Energy **177**, 1346–1355 (2021). https://doi.org/10.1016/j.renene.2021.06.005
17. H. Park, E. Lee, M. Lei, H. Joo, S. Coh et al., Canonic-like HER activity of $Cr_{1-x}Mo_xB_2$ solid solution: overpowering Pt/C at high current density. Adv. Mater. **32**(28), 2000855 (2020). https://doi.org/10.1002/adma.202000855
18. Y. Liu, S.B. Yin, P.K. Shen, Asymmetric 3d electronic structure for enhanced oxygen evolution catalysis. ACS Appl. Mater. Interfaces **10**(27), 23131–23139 (2018). https://doi.org/10.1021/acsami.8b06106
19. Y.B. Li, X. Tan, H. Tan, H.J. Ren, S. Chen et al., Phosphine vapor-assisted construction of heterostructured $Ni_2P/NiTe_2$

catalysts for efficient hydrogen evolution. Energy Environ. Sci. **13**(6), 1799–1807 (2020). https://doi.org/10.1039/d0ee00666a

20. Y. Gu, S. Chen, J. Ren, Y.A. Jia, C.M. Chen et al., Electronic structure tuning in Ni_3FeN/r-GO aerogel toward bifunctional electrocatalyst for overall water splitting. ACS Nano **12**(1), 245–253 (2018). https://doi.org/10.1021/acsnano.7b05971
21. D. Lyu, Y. Du, S. Huang, B.Y. Mollamahale, X. Zhang et al., Highly efficient multifunctional Co-N-C electrocatalysts with synergistic effects of Co-N moieties and Co metallic nanoparticles encapsulated in a N-doped carbon matrix for water-splitting and oxygen redox reactions. ACS Appl. Mater. Interfaces **11**(43), 39809–39819 (2019). https://doi.org/10.1021/acsami.9b11870
22. D.H. Deng, K.S. Novoselov, Q. Fu, N.F. Zheng, Z.Q. Tian et al., Catalysis with two-dimensional materials and their heterostructures. Nat. Nanotechnol. **11**, 218–230 (2016). https://doi.org/10.1038/nnano.2015.340
23. C. Panda, P.W. Menezes, S. Yao, J. Schmidt, C. Walter et al., Boosting electrocatalytic hydrogen evolution activity with a $NiPt_3$@NiS heteronanostructure evolved from a molecular nickel-platinum precursor. J. Am. Chem. Soc. **141**(34), 13306–13310 (2019). https://doi.org/10.1021/jacs.9b06530
24. S.S. Wang, Y.C. Xu, R.R. Fu, H.H. Zhu, Q.Z. Jiao et al., Rational construction of hierarchically porous Fe-Co/N-doped carbon/rGO composites for broadband microwave absorption. Nano-Micro Lett. **11**, 76 (2019). https://doi.org/10.1007/s40820-019-0307-8
25. X. Luo, P.X. Ji, P.Y. Wang, R.L. Cheng, D. Chen et al., Interface engineering of hierarchical branched Mo-doped Ni_3S_2/Ni_xP_y hollow heterostructure nanorods for efficient overall water splitting. Adv. Energy Mater. **10**(17), 1903891 (2020). https://doi.org/10.1002/aenm.201903891
26. F. Lin, Z.H. Dong, Y.H. Yao, L. Yang, F. Fang et al., Electrocatalytic hydrogen evolution of ultrathin Co-Mo_5N_6 heterojunction with interfacial electron redistribution. Adv. Energy Mater. **10**(42), 2002176 (2020). https://doi.org/10.1002/aenm.202002176
27. J.J. Lu, S.B. Yin, P.K. Shen, Carbon-encapsulated electrocatalysts for the hydrogen evolution reaction. Electrochem. Energy Rev. **2**, 105–127 (2018). https://doi.org/10.1007/s41918-018-0025-9
28. Y.C. Tu, P.J. Ren, D.H. Deng, X.H. Bao, Structural and electronic optimization of graphene encapsulating binary metal for highly efficient water oxidation. Nano Energy **52**, 494–500 (2018). https://doi.org/10.1016/j.nanoen.2018.07.062
29. A. Saad, H.J. Shen, Z.X. Cheng, R. Arbi, B.B. Guo et al., Mesoporous ternary nitrides of earth-abundant metals as oxygen evolution electrocatalyst. Nano-Micro Lett. **12**, 79 (2020). https://doi.org/10.1007/s40820-020-0412-8
30. S. Xue, Z.B. Liu, C.Q. Ma, H.M. Cheng, W.C. Ren, A highly active and durable electrocatalyst for large current density hydrogen evolution reaction. Sci. Bull. **65**(2), 123–130 (2020). https://doi.org/10.1016/j.scib.2019.10.024
31. A. Kumar, V.Q. Bui, J.Y. Lee, A.R. Jadhav, Y. Hwang et al., Modulating interfacial charge density of NiP_2-FeP_2 via coupling with metallic Cu for accelerating alkaline hydrogen evolution. ACS Energy Lett. **6**(2), 354–363 (2021). https://doi.org/10.1021/acsenergylett.0c02498
32. A. Manikandan, L. Lee, Y.C. Wang, C.W. Chen, Y.Z. Chen et al., Graphene-coated copper nanowire networks as a highly stable transparent electrode in harsh environments toward efficient electrocatalytic hydrogen evolution reactions. J. Mater. Chem. A **5**(26), 13320–13328 (2017). https://doi.org/10.1039/c7ta01767g
33. D.T. Tran, H.T. Le, V.H. Hoa, N.H. Kim, J.H. Lee, Dual-coupling ultrasmall iron-Ni_2P into P-doped porous carbon sheets assembled Cu_xS nanobrush arrays for overall water splitting. Nano Energy **84**, 105861 (2021). https://doi.org/10.1016/j.nanoen.2021.105861
34. Y.T. Wu, H. Wang, S. Ji, B.G. Pollet, X.Y. Wang et al., Engineered porous Ni_2P-nanoparticle/Ni_2P-nanosheet arrays via the Kirkendall effect and Ostwald ripening towards efficient overall water splitting. Nano Res. **13**, 2098–2105 (2020). https://doi.org/10.1007/s12274-020-2816-7
35. Y.M. Zhao, X.W. Wang, G.Z. Cheng, W. Luo, Phosphorus-induced activation of ruthenium for boosting hydrogen oxidation and evolution electrocatalysis. ACS Catal. **10**(20), 11751–11757 (2020). https://doi.org/10.1021/acscatal.0c03148
36. V.L. Deringer, U. Englert, R. Dronskowski, Covalency of hydrogen bonds in solids revisited. Chem. Commun. **50**(78), 11547–11549 (2014). https://doi.org/10.1039/c4cc04716h
37. X. Liu, K. Ni, B. Wen, C.J. Niu, J.S. Meng et al., Polyoxomolybdate-derived carbon-encapsulated multicomponent electrocatalysts for synergistically boosting hydrogen evolution. J. Mater. Chem. A **6**(37), 17874–17881 (2018). https://doi.org/10.1039/c8ta07135g
38. H. Han, K.M. Kim, J.H. Ryu, H.J. Lee, J. Woo et al., Boosting oxygen evolution reaction of transition metal layered double hydroxide by metalloid incorporation. Nano Energy **75**, 104945 (2020). https://doi.org/10.1016/j.nanoen.2020.104945
39. D. Chen, T.T. Liu, P.Y. Wang, J.H. Zhao, C.T. Zhang et al., Ionothermal route to phase-pure RuB_2 catalysts for efficient oxygen evolution and water splitting in acidic media. ACS Energy Lett. **5**(9), 2909–2915 (2020). https://doi.org/10.1021/acsenergylett.0c01384
40. X.H. Wan, H.A. Niu, Y.H. Yin, X.T. Wang, C. Shao et al., Enhanced electrochemical oxygen evolution reaction activity on natural single-atom catalysts transition metal phthalocyanines: the substrate effect. Catal. Sci. Technol. **10**(24), 8339–8346 (2020). https://doi.org/10.1039/d0cy01651a
41. F.N. Yang, Y.T. Luo, Q.M. Yu, Z.Y. Zhang, S. Zhang et al., A durable and efficient electrocatalyst for saline water splitting with current density exceeding 2000 mA cm^{-2}. Adv. Funct. Mater. **31**(21), 2010367 (2021). https://doi.org/10.1002/adfm.202010367
42. G.F. Qian, J.L. Chen, T.Q. Yu, L. Luo, S.B. Yin, N-doped graphene-decorated NiCo alloy coupled with mesoporous NiCo-MoO nano-sheet heterojunction for enhanced water electrolysis activity at high current density. Nano-Micro Lett. **13**, 77 (2021). https://doi.org/10.1007/s40820-021-00607-5
43. Y.P. Li, J.H. Zhang, Y. Liu, Q.Z. Qian, Z.Y. Li et al., Partially exposed RuP_2 surface in hybrid structure endows its

 https://doi.org/10.1007/s40820-021-00744-x

bifunctionality for hydrazine oxidation and hydrogen evolution catalysis. Sci. Adv. (2020). https://doi.org/10.1126/sciadv.abb4197

44. L. Pei, J.S. Zhong, T.Z. Li, W.F. Bai, S.T. Wu et al., CoS_2@N-doped carbon core-shell nanorod array grown on Ni foam for enhanced electrocatalytic water oxidation. J. Mater. Chem. A **8**(14), 6795–6803 (2020). https://doi.org/10.1039/d0ta00777c
45. Q.Z. Qian, J.H. Zhang, J.M. Li, Y.P. Li, X. Jin et al., Artificial heterointerfaces achieve delicate reaction kinetics towards hydrogen evolution and hydrazine oxidation catalysis. Angew. Chem., Int. Ed. **60**(11), 5984–5993 (2021). https://doi.org/10.1002/anie.202014362
46. S.Y. Jing, L.S. Zhang, L. Luo, J.J. Lu, S.B. Yin et al., N-doped porous molybdenum carbide nanobelts as efficient catalysts for hydrogen evolution reaction. Appl. Catal. B **224**, 533–540 (2018). https://doi.org/10.1016/j.apcatb.2017.10.025
47. D. Zhao, K. Sun, W.C. Cheong, L.R. Zheng, C. Zhang et al., Synergistically interactive pyridinic-N-MoP sites: Identified active centers for enhanced hydrogen evolution in alkaline solution. Angew. Chem., Int. Ed. **59**(23), 8982–8990 (2020). https://doi.org/10.1002/anie.201908760
48. G.C. Yang, Y.Q. Jiao, H.J. Yan, Y. Xie, A.P. Wu et al., Interfacial engineering of MoO_2-FeP heterojunction for highly efficient hydrogen evolution coupled with biomass electrooxidation. Adv. Mater. **32**(17), 2000455 (2020). https://doi.org/10.1002/adma.202000455
49. Q. Zhang, W. Chen, G.L. Chen, J. Huang, C.S. Song et al., Bi-metallic nitroxide nanodot-decorated tri-metallic sulphide nanosheets by on-electrode plasma-hydrothermal sprouting for overall water splitting. Appl. Catal. B **261**, 118254 (2020). https://doi.org/10.1016/j.apcatb.2019.118254
50. H.J. Yan, Y. Xie, A.P. Wu, Z.C. Cai, L. Wang et al., Anion-modulated HER and OER activities of 3D Ni-V-based interstitial compound heterojunctions for high-efficiency and stable overall water splitting. Adv. Mater. **31**(23), 1901174 (2019). https://doi.org/10.1002/adma.201901174
51. D.R. Wang, J.J. Lu, L. Luo, S.Y. Jing, H.S. Abbo et al., Enhanced hydrogen evolution activity over microwave-assisted functionalized 3D structured graphene anchoring FeP nanoparticles. Electrochim. Acta **317**, 242–249 (2019). https://doi.org/10.1016/j.electacta.2019.05.153
52. X.R. Gao, X.M. Liu, W.J. Zang, H.L. Dong, Y.J. Pang et al., Synergizing in-grown Ni_3N/Ni heterostructured core and ultrathin Ni_3N surface shell enables self-adaptive surface reconfiguration and efficient oxygen evolution reaction. Nano Energy **78**, 105355 (2020). https://doi.org/10.1016/j.nanoen.2020.105355
53. X. Liu, R.T. Guo, K. Ni, F.J. Xia, C.J. Niu et al., Reconstruction-determined alkaline water electrolysis at industrial temperatures. Adv. Mater. **32**(40), 2001136 (2020). https://doi.org/10.1002/adma.202001136
54. X. Liu, J.S. Meng, K. Ni, R.T. Guo, F.J. Xia et al., Complete reconstruction of hydrate pre-catalysts for ultrastable water electrolysis in industrial-concentration alkali media. Cell Rep. Phys. Sci. **1**(11), 100241 (2020). https://doi.org/10.1016/j.xcrp.2020.100241
55. Z.Y. Yu, C.C. Lang, M.R. Gao, Y. Chen, Q.Q. Fu et al., Ni-Mo-O nanorod-derived composite catalysts for efficient alkaline water-to-hydrogen conversion via urea electrolysis. Energy Environ. Sci. **11**(7), 1890–1897 (2018). https://doi.org/10.1039/c8ee00521d
56. M.Y. Zu, C.W. Wang, L. Zhang, L.R. Zheng, H.G. Yang, Reconstructing bimetallic carbide Mo_6Ni_6C for carbon interconnected MoNi alloys to boost oxygen evolution electrocatalysis. Mater. Horiz. **6**(1), 115–121 (2019). https://doi.org/10.1039/c8mh00664d
57. X.D. Cheng, C.J. Lei, J. Yang, B. Yang, Z.J. Li et al., Efficient electrocatalytic oxygen evolution at extremely high current density over 3D ultrasmall zero-valent iron-coupled nickel sulfide nanosheets. ChemElectroChem **5**(24), 3866–3872 (2018). https://doi.org/10.1002/celc.201801104
58. Y. Tan, Q. Li, Q.J. Che, X.H. Chen, X. Xu et al., Improving activity of Ni_3P/Mn hybrid film via electrochemical tuning for water splitting under simulated industrial environment. Electrochim. Acta **324**, 134897 (2019). https://doi.org/10.1016/j.electacta.2019.134897
59. D.S. Raja, X.F. Chuah, S.Y. Lu, In situ grown bimetallic MOF-based composite as highly efficient bifunctional electrocatalyst for overall water splitting with ultrastability at high current densities. Adv. Energy Mater. **8**(23), 1801065 (2018). https://doi.org/10.1002/aenm.201801065
60. X.F. Chuah, C.T. Hsieh, C.L. Huang, D.S. Raja, H.W. Lin et al., In-situ grown, passivator-modulated anodization derived synergistically well-mixed Ni-Fe oxides from Ni foam as high-performance oxygen evolution reaction electrocatalyst. ACS Appl. Energy Mater. **2**(1), 743–753 (2018). https://doi.org/10.1021/acsaem.8b01794
61. Z.C. Wu, Z.X. Zou, J.S. Huang, F. Gao, $NiFe_2O_4$ nanoparticles/NiFe layered double-hydroxide nanosheet heterostructure array for efficient overall water splitting at large current densities. ACS Appl. Mater. Interfaces **10**(31), 26283–26292 (2018). https://doi.org/10.1021/acsami.8b07835
62. C.L. Huang, X.F. Chuah, C.T. Hsieh, S.Y. Lu, NiFe alloy nanotube arrays as highly efficient bifunctional electrocatalysts for overall water splitting at high current densities. ACS Appl. Mater. Interfaces **11**(27), 24096–24106 (2019). https://doi.org/10.1021/acsami.9b05919
63. Q.J. Che, Q. Li, Y. Tan, X.H. Chen, X. Xu et al., One-step controllable synthesis of amorphous (Ni-Fe)S_x/$NiFe(OH)_y$ hollow microtube/sphere films as superior bifunctional electrocatalysts for quasi-industrial water splitting at large-current-density. Appl. Catal. B **246**, 337–348 (2019). https://doi.org/10.1016/j.apcatb.2019.01.082
64. X.D. Cheng, Z.Y. Pan, C.J. Lei, Y.J. Jin, B. Yang et al., A strongly coupled 3D ternary Fe_2O_3@Ni_2P/$Ni(PO_3)_2$ hybrid for enhanced electrocatalytic oxygen evolution at ultra-high current densities. J. Mater. Chem. A **7**(3), 965–971 (2019). https://doi.org/10.1039/c8ta11223a
65. J.X. Yuan, X.D. Cheng, H.Q. Wang, C.J. Lei, S. Pardiwala et al., A superaerophobic bimetallic selenides heterostructure for efficient industrial-level oxygen evolution at ultra-high current densities. Nano-Micro Lett. **12**, 104 (2020). https://doi.org/10.1007/s40820-020-00442-0